UNIVERSIDAD COMPLUTENSE DE MADRID

FACULTAD DE CIENCIAS FÍSICAS

DEPARTAMENTO DE ESTRUCTURA DE LA MATERIA, FÍSICA TÉRMICA Y ELECTRÓNICA

TRABAJO DE FIN DE GRADO

Código de TFG: ETE42

Introducción a la Astrofísica de Muy Altas Energías

Introduction to Very High Energy Astrophysics

Supervisores: Atreyee Sinha y José Luis Contreras González

Jorge Buces Sáez

Grado en Física

Curso académico 2021-2022

Convocatoria de Junio

Resumen:

Este trabajo es una introducción a la física de los Núcleos de Galaxias Activos (AGN), en particular a los blazars y a su emisión en altas energías. Los blazars, que son AGNs con un jet relativista orientado en la dirección de la línea de visión del observador, son una de las fuentes más numerosas de emisión en Muy Altas Energías (VHE; por encima de los 100 GeV) del universo. A pesar de la gran cantidad de literatura disponible sobre estos objetos, el origen de esta emisión en altas energías sigue siendo objeto de debate. Empezaremos con una breve introducción a los AGNs y a los procesos radiativos leptónicos que mejor simulan el espectro de estos blazars. Posteriormente, veremos las técnicas experimentales que nos permiten detectar de manera directa o indirecta estos fotones. Finalmente, usando el modelo leptónico, haremos un estudio de caso del estado de flare observado en Abril del 2011 en Markarian 421, uno de los emisores extragalácticos más estudiado en altas energías.

Abstract:

This work is an introduction to the physics of Active Galactic Nuclei (AGN), particularly to blazars and their high-energy emission. Blazars, which are AGNs with a relativistic jet pointing towards the line of sight of the observer, count among the most numerous sources of Very High Energy (VHE; above 100 GeV) emission in the universe. Despite the vast amount of literature available on these objects, the origin of the high energy emission remains under debate. We will begin with a brief description of AGNs and the main radiative leptonic processes that best simulate their spectrum. Subsequently, we will look at experimental techniques for detecting this type of photons. And finally we will make a case study of a flare occurred in April 2011, in one of the best known high-energy extragalactic emitters: Markarian 421, making use of a leptonic model.

Contents

1 Introduction

The study of the sky is one of the oldest branches of physics, the observation of which has captivated mankind since ancient times. Despite this, however, there are still countless unanswered questions. Beyond its study for the wider knowledge of the universe, the processes produced in these environments allow us to approach energies still unattainable in laboratories nowadays. In this work, we will study one of these Very High Energy emitters, the AGNs. We consider the VHE range from 100 GeV up to 100 TeV. Active Galactic Nuclei constitute the most abundant and persistent source of extragalactic very high energy radiation. Modelling this emission with the radiative processes of relativistic charged particles allows one to derive their non-thermal energy distributions, to infer their acceleration mechanism and site, and to investigate the jet composition.

2 Active Galactic Nuclei

2.1 Introduction on AGNs

It is known that in our universe some galaxies have very bright nuclei, which emit intense radiation along the whole electromagnetic spectrum, outshining their hosting galaxies. They are called Active Galaxies, and their core Active Galactic Nuclei (AGN) or Quasar. The name Quasar comes from quasi-stellar object due to their incredibly bright nuclei, which can be brighter than all the stars in the galaxy (10^{11} $L_\odot$) by a factor 100 or more, thus we can remove the highlighted portion. They also have a rapidly varying luminosity which gives us two clearly distinguishable states, the low activity, called the quiescent state, and multiple high activity states with varying characteristics, this will be discussed in section 4.1. Quasars are characterised by a very broad Spectral Energy Distribution (SED), a rapid and large amplitude variability in optical and radio emission (with time scale ranging from minutes to days) and are among the most luminous objects at all wavelengths.

AGNs have been observed and classified from the early 20th century. Experimentally, we can divide them into two principal groups: radio quiet (Seyfert galaxies), and radio loud sources of different types, depending on whether they show activity in radio observations or not. The two groups also show differences in the luminosity of their central source. Along the years a unified model of AGNs has beeen developed, this model indicates that the main differences between the different types of AGNs is not morphological, but depends on the viewing angle of the observer. Depending on the orientation, certain elements such as the dust toroid will obscure some emission regions such as the Broad Line Reigion. According to it, AGNs host a supermassive black hole (SMBH) ($M > 10^7$ $M_\odot$) in the center, fed by a hot accretion disk of matter, which in turn is surrounded by a dusty torus and two zones of clouds. The Broad Line region (BLR) zone that is an inner, small zone, with dense and fast moving clouds, and the Narrow Line Region (NLR) which is larger, and contains slower and less dense rarefied clouds of ionized gas, with a total size of 10 to 1,000 parsecs. More about the taxonomy can be seen in [4]. A sketch of this model is represented in figure 1.

Radio quiet sources are subdivided into two groups, Seyfert 1 and Seyfert 2 galaxies. Nearly all Seyferts are spiral galaxies. But the kind of AGNs which we are going to focus on is radio loud AGNs, which are classified in 3 categories Narrow Line Radio Galaxies, Broad Line Radio Galaxies and Blazars. They usually have an impressive, collimated jet of ultra-relativistic particles with a length comparable to the size of a galaxy, ranging up to Mpc scales. Though the exact origin of these jets is still unknown, it is thought to be launched by the magnetic field of the accretion disk that accelerates particles in the surroundings of the black hole. The particles themselves contribute to this magnetic field. The interests on this megastructures arises from the fact that this powerful emission hides very highly energetic processes. Furthermore the emission from jets doesn't have a
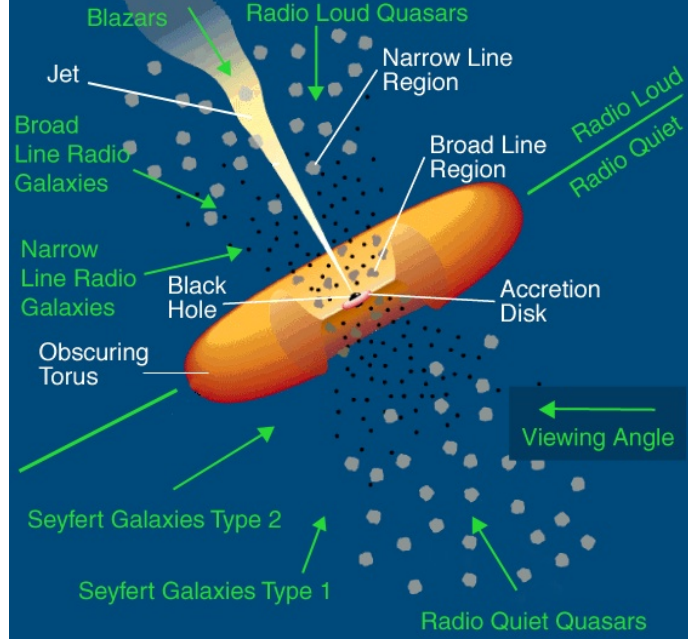
Figure 1: Components and galaxy types according to the unified model of AGN. Taken from reference [24]

thermal origin, and therefore doesn't follow a black body distribution as in the case of stars. The main candidate to explain these spectra is the emission from high energy particles either leptons or hadrons. Specifically blazars are radio loud sources with the jet pointing towards us, their apparent luminosity can reach 10^{49} erg/s due to extreme relativistic aberration, and it is among the most violent sources of high energy emission. They present a double hump in its spectrum, figure 2, one of the humps is located in the IR-X-ray regime and the other in the gamma ray regime. Some of these photons may be absorbed by the intergalactic medium, thus attenuating the received spectrum, this will be explained in section 2.3.
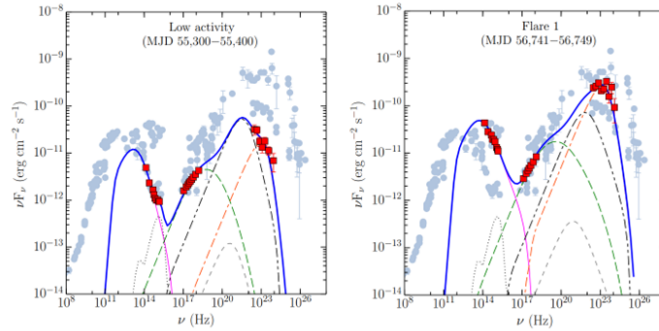
Figure 2: SED of 3C 279 during low and high activity states, from [23]

Supposing that this huge amount of energy expelled is created by converting gravitational energy into radiation, it can be seen that there is a minimum mass called Eddington Mass [24] for the AGN, given by:

$$M_E = 8 \cdot 10^5 L_{44} M_\odot \tag{1}$$

With L_{44} the luminosity in units of 10^{44} $erg \cdot s^{-1}$. Later on, in section 4 we will study the

case of the blazar Markarian 421, knowing the flux (0.3 crab units, according to [20]), with a few calculations using equation 1 we can obtain it minimum mass for its SMBH of $M_E = 1.2 \cdot 10^8 M_\odot$.

2.2 Main radiative processes in blazars

As we have seen in the previous section, there is a distinctive double hump in blazar spectra (fig. 2). In the scientific community there is not a total agreement on which radiative processes are behind the second peak, probably a sum of leptonic and hadronic processes. Nevertheless Synchrotron Self Compton (SSC) and Inverse Compton (IC) seem to fit quite well this part of the spectrum, so those are the ones that we are going to focus on.

- Synchrotron:
  Particles moving in a weak magnetic field $\vec{B}$ will radiate with the frecuency of gyration in the magnetic field, it is called cyclotron radiation. In a strong magnetic field this will not be the case anymore. Particles entering the magnetic field have extreme relativistic velocities, and as we are going to see, magnetic field will apply a huge normal acceleration implying a helical motion. The radiation emitted by the electrons is called synchrotron radiation.
  We can obtain the kinematics of the particle by supposing that there is only a magnetic field, and so, as $\vec{B}$ does not accomplish any work on the particle, energy will be conserved:

$$\frac{dW}{dt} = \vec{F} \cdot \vec{v} \rightarrow \frac{d(\gamma mc^2)}{dt} = 0 \tag{2}$$

Where $\vec{F}$ is the electromagnetic force, $\vec{v}$ the speed of the particle and m its mass. Equation 2 implies that the Lorentz factor $\gamma = \frac{1}{\sqrt{1-v^2/c^2}}$ and the module of the speed v are constant.

With no loss of generality we take $\vec{B}$ in the z axis, and we can obtain :

$$\frac{d\vec{p}}{dt} = \vec{F} \rightarrow \frac{d(\gamma m\vec{v})}{dt} = \frac{q}{c}(\vec{v} \times \vec{B}) \rightarrow \frac{d\vec{v}}{dt} = \frac{qB}{\gamma mc}(\vec{v} \times \hat{z}) = \omega_B(\vec{v} \times \vec{z}) \tag{3}$$

$$\omega_B = \frac{qB}{\gamma mc} \tag{4}$$

Where q is the charge of the particle and ω_B the cyclotron frecuency, which is the frecuency of rotation. As the speed is constant, what will change with time is its direction. These equations give raise to a circular motion in the x,y plane and constant velocity in the z plane. The acceleration is then perpendicular to the velocity with constant value $a_\perp = \omega_B \cdot v_\perp$.
The total emitted radiation by a moving particle is in this situation given by [15]:

$$P = \frac{2q^2}{3c^3}\gamma^4(a_\perp^2 + \gamma^2 a_\parallel^2) = \frac{2q^2}{3c^3}\gamma^4\omega_B^2 v_\perp^2 \tag{5}$$

For an isotropic distribution of velocities, averaging over all α, the angle between $\vec{B}$ and $\vec{v}$:

$$P = \frac{4}{9}r_e^2 c\beta^2\gamma^2 B^2 = \frac{4}{3}\sigma_T c\gamma^2\beta^2 U_B \approx 1.06 \cdot 10^{-15}\gamma^2\left(\frac{B}{1G}\right)^2 \tag{6}$$

Where $r_e = e/4\pi m_e^2 c^2$ is the classical electron radius, $\sigma_T = 8\pi r_0^2/3$ the Thomson scattering cross section and $U_B = B^2/8\pi$ the magnetic energy density. The emited radiation is focused

in a cone of solid angle proportional to γ^{-1}. In an extreme relativistic case, as it is for blazars ($\beta \approx 1$), the power per unit frequency radiated by each electron is:

$$\frac{dW}{d\omega dt} = P(\omega) = \frac{\sqrt{3}q^3 B sin\alpha}{2\pi mc^2} F(\frac{\omega}{\omega_c})$$ (7)

With $\omega_c = (3/2)\gamma^2 \omega_B sin\alpha$ the critical frecuency and $F(x)$ a dimensionless function with a maximum reached for $x = 0.29$. Assuming a density of relativistic electrons which follows the law $N(\gamma)d\gamma = k \cdot \gamma^{-p}d\gamma$ we can obtain the total power, which is proportional to $\omega^{-\frac{p-1}{2}}$.

- Inverse Compton:
  Electrons and photons can interact in different ways, one of those ways is Inverse Compton (IC), where an energetic electron finds a low energy photon in its way. In this case a fraction of the energy of the electron will be transfered to the photon. For a single electron and assuming a photon density in the range of energies $d\epsilon$ given by $vd\epsilon$ with isotropic distribution, we can calculate the rate of change of the energy by unit of time of the electron, that will be converted in radiation. Obtaining the total power radiated by Compton effect for a single electron [27]:

$$P_{compt} = \frac{dE_{rad}}{dt} = \frac{4}{3}\sigma_T c\gamma^2 \beta^2 U_{ph}$$ (8)

With $U_{ph} = \int \epsilon v d\epsilon$ is the initial photon energy density, γ the Lorentz factor of the electron, and σ_T the Thomson cross section which is the probability of having this scattering whithin the Thomson regime ($\gamma h\nu \ll m_e c^2$). We can imagine two principal cases.
The first in which the photon energy is low compared with the rest energy of the electron and we can ignore the electron recoil, assuming an elastic scattering, this is the Thomson regime. The scattered photon energy will be $\epsilon_s \approx \gamma^2 \epsilon$. The differential cross section is given by:

$$\frac{d\sigma_T}{d\Omega} = \frac{1}{2}r_e^2(1 + cos^2\theta)$$ (9)

With θ the angle between the incoming photon and the scattered one. For an isotropic distribution of electrons and photons, the shape of the spectrum will be given by the scattered power per volume (V) per energy:

$$\frac{dE}{dVd\epsilon dt} = 4\pi\epsilon j(\epsilon) = \frac{k8\pi^2 r_e^2}{h^3 c^2}(k_B T)^{(p+5)/2}F(p)\epsilon^{-(p-1)/2}$$ (10)

It will then have the same dependence in ω as the synchrotron radiation. With $j(\epsilon)$ the emission function and supposing an initial photon number density distribution propper of a blackbody with temperature T.
The second case, where the electron recoil is considerable,is called the Klein-Nishina regime ($\gamma h\nu \gg m_e c^2$). In order to calculate its differential cross section we will need to use QED theory, obtaining:

$$\frac{d\sigma_{K_N}}{d\Omega} = \frac{r_e^2 \epsilon_s^2}{2\epsilon^2}\left(\frac{\epsilon}{\epsilon_s} + \frac{\epsilon_s}{\epsilon} - sin^2\theta\right)$$ (11)

Which in the Thomson limit is equal to $\frac{d\sigma_T}{d\Omega}$. In extreme K-N regime, the electron loses almost its entire energy in a single Compton scattering, in contrast to the Thomson regime where the electron loses it energy through many small interactions. The scattered photon energy will be $\epsilon_s \gg \gamma m_e c^2$. And its spectrum will behave as ϵ^{-p}.
In the Synchrotron-Self Compton (SSC) process, the scattered photons come from the synchrotron radiation. That is, the electrons emitting by synchrotron effect will themselves

scatter those photons. It can be seen that for a power law electron distribution as seen in the previous section, the spectrum will follow the a power law with the index going from the Thomson regime to the K-N regime, depending on the frequency of the photon.

Electrons accelerated by the magnetic field can also scatter ambient photon, this process is called External Compton (EC). Those ambient photons may come from various places, as the Extragalactic Background Light (EBL), the AGN torus, or the Cosmic Microwave Background (CMB).

2.3   Absorption

As we have seen, gamma ray photons can be produced in different ways in blazars. Because of their high luminsity, these objects can be detected at cosmological distances. However, some of these highly energetic photons will not reach us. This loss of information is due to the distance from the source, the intergalactic medium that separates us from the AGN, and the energy of the emitted photons, as they are not all absorbed in the same way. One of the main cause of this loss of information is absorption by photon-photon interaction. When an energetic gamma-ray photon finds a less energetic photon (optical-IR) in its way, they may interact anihilating themselves and producing a pair of an electron and a positron as:

$$\gamma + \gamma \longrightarrow e^+ + e^- \tag{12}$$

The threshold energy for the creation of an $e^+ - e^-$ pair is given by:

$$E_{th} = 2\frac{(m_e c^2)^2}{E_\gamma(1 - cos\theta)} \tag{13}$$

With θ the angle between the two photons. After the CMB, the EBL is the brightest radiative field, it behaves as a photon gas, its spectrum extends from the near UV to the far IR, the range of energy in which γ photons may be scattered. These photons are produced direct or indirectly by stars (by heating intergalactic dust that will after emit photons), they are the light that spans among galaxies. The EBL can be estimated by direct measurements such as direct observations or cosmological models using star formation observations and the number of galaxies. These methods are difficult due to the strong foreground emission. Therefore, indirect measurements using blazars are also employed.By analyzing several blazar spectra, with different redshifts and intensities, it has been possible to establish upper and lower limits to this EBL, for details see [9]. With a deeper knowledge of this photon background, we will be able to get a better awareness of the intrinsic properties of AGN's. Moreover, the study on the EBL is important, because it contains the history of the emission of light by all bodies in the universe.

3   Data sources and tools

3.1   Observatories

In this section we briefly summarize the different types of data we have used and their origin.

Our atmosphere is opaque to gamma rays and X-rays, making it impossible to detect high energy photons directly from Earth. Two solutions to this problem were found. The first one, and most intuitive, was to send telescopes into space, in order to avoid extinction caused by the atmosphere. The second one, only valid for VHE radiation, is the detection of secondary particles and light from the ground, coming from the so called Extensive Air Showers (EAS).
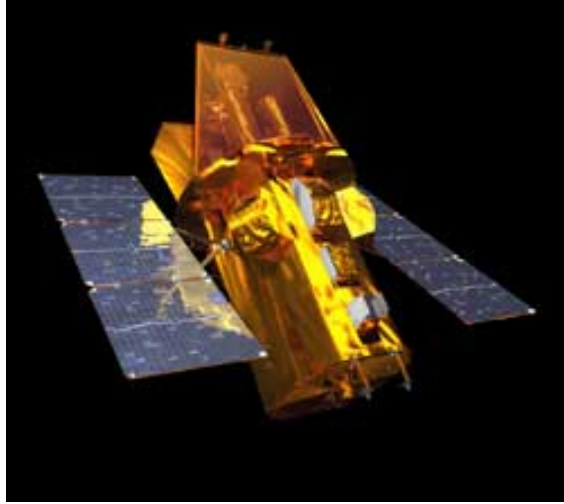
The source of the X-ray data used in this work is the Swift satellite [32]. It is a multiwavelength satellite covering from optical-UV to X-ray, and its fast response makes it capable to detect GRBs.

Launched on November 2004, in an orbit of 595 km of altitude, and a period of 97 minutes, it carries three instruments on board. The first instrument is the Ultraviolet/Optical Telescope (UVOT), with 3 optical filters U, B, V and 3 UV filters UVW1, UVM1, UVW2. The X-ray Telescope (XRT) with 110 cm^2 effective area, and an energy range of 0.2 to 10 keV, has the aim to conduct the most sensitive all-sky survey in astronomical X-ray sources. The Burst Alert Telescope (BAT), it operates over the 15-150 keV energy range, with a telescope effective area of 5240 cm^2, has the goal of determine the origin of GRB, and study the early universe. Another telescope used for the X-ray data used in this work is the NuSTAR (Nuclear Spectroscopic Telescope Array). This telescope captures photons in the 3 to 80 keV range, and was launched on June 13, 2012, for more information about NuSTAR [22].

(a) Fermi telescope from [30]   (b) Swift telescope from [32]

Figure 3: Fermi and Swift telescopes

In the gamma-ray range, the Fermi Gamma ray space telescope spacecraft is the most powerful observatory ever built[30]. It resides in a low-Earth orbit at an altitude of 550km, with a short orbit period (95 mins), and observes a 20% of the sky at any given time. Launched on june 2008, it carries two principal instruments, the main one is the Fermi Large Area Telescope (LAT), it is an imaging gamma ray detector which operates in range of 20 MeV to 300 GeV. It is based in pair production. The other instrument is called the Fermi Gamma ray Burst Monitor (GBM) and is able to detect gamma ray bursts from 8 keV to 30 MeV acroos the whole sky.
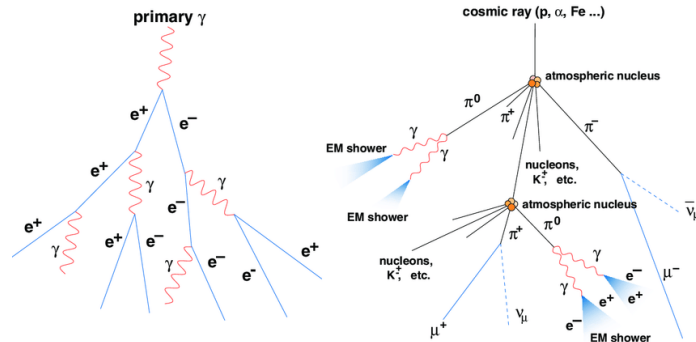

Figure 4: Electromagnetic EAS (left), and hadronic cascade (right) taken from [18]

For VHE photons (energies from a few GeV to a hundred TeV), the method of particle detection at ground level is used, via EAS. There are two types of EAS, those of electromagnetic origin and those of hadronic origin. The electromagnetic ones are originated by primary gamma rays or electrons. When a gamma ray interacts with the atmosphere ir produces a pair of very energetic e^-e^+, which can in turn radiate through the bremsstrahlung effect. These photons will in turn create a new e^-e^+ pair again, this process will go on in the athmosphere, creating each time less energetic particles, until the energy is such that no new particles are produced and the created ones are absorbed in the atmosphere. If the energy is large enough the cascade of particles arrives to the ground as a large disk. The other kind are the EAS are produced by cosmic rays, protons or heavier nuclei, when they interact with atmospheric nuclei they will produce hadrons, that again will interact with other air molecules and produce new mesons and baryons. These EAS can also have electromagnetic particles, due to the decay of the π^0s in a pair of photons, $\pi^\pm$s and kaon decays also produce leptons among which there are electrons. A scheme of the development of an electromagnetic and a hadronic EAS is shown in figure 4

For energíes below 100 GeV EAS processes will stop at an altitude of around 10 km, while for higher energies, secondary particles can reach the Earth surface. Nevertheless, in the second case the Cherenkov radiation produced by relativistic charged particles in the EAS will reach the ground and so it is possible to detect them. These new photons with energies that go from the UV to the visible, can be collected with telescopes at Earth. Cherenkov light from EAS forms a cone around the EAS direction, its typical radius at ground is 120 m. A telescope inside this radius will detect the Cherenkov light. Those telescopes are called Imaging Atmospheric Cherenkov Telescopes (IACT). Cherenkov observatories include the Major Atmospheric Gamma Imaging Cherenkov Telescopes (MAGIC) in La Palma [31], the High Energy Stereoscopic System (H.E.S.S.)[14] in Namibia, and the Very Energetic Radiation Imaging Telescope Array System (VERITAS)[33] in USA. They are systems of telescopes spaced a hundred metres apart that, starting from the Cherenkov light collected are able to reconstruct the shower and from it the energy and direction of the particle the originated it.

In this work we have used data from the MAGIC observatory, a set of two Cherenkov telescopes of 17 m diameter each. It covers energies from 20 GeV to over 100 TeV. A photograpph of MAGIC can be seen in figure 5.

3.2 Software tools

The aim of this project is to model the broadband spectrum of a specific blazar, Mkn421, during different flux states. For this, we are going to use two principal open source python packages, gammapy for data analysis, and agnpy for modeling the SED of the AGN.

Agnpy [3] is a relatively new open-source package used to model the AGN SED by thermal and non-thermal emission processes. It represents one of the first systematic and validated collection of established radiative processes for jetted active galaxies. Starting from a blob, which is a plasmoid sphere with a number of properties that we will see later, such as its size, velocity, magnetic field, and the spectral distribution of electrons among others, Agnpy will calculate the observed emission from synchrotron, SSC and EC processes, while correcting for beaming effects. It can also take into account the absorption due to EBL. It is also possible to model thermal emission zones such as the dusty torus, or the disc, which will represent the origin of photons to recreate other non-thermal processes such as the inverse Compton or the SSC, more information about agnpy can be found in [21].

Gammapy is an open-source Python package for gamma-ray astronomy data analysis [12], which provides support for both data reduction and high level modelling and fitting. Gammapy is widely used, recommended by the H.E.S.S. observatory, and used in MAGIC and VERITAS for example,

Figure 5: The MAGIC telescopes at La Palma. Credit: Chiara Righi. The MAGIC Collaboration, taken from [11]

more about gammapy can be found in [7].

We will use gammapy in parallel with agnpy, i.e. first using the calculation and other models already created, to estimate some initial parameters. Then we will use this package to fit these initially estimated parameters. Traditionally, due to the complicated parameter estimation, underlying physical parameters were simply obtained through eye-ball estimation ([2], [1]). Now, with the availability of high quality data from these experiments through coordinated multi wavelength observations and improved computational resources, it is possible to perform a statistical fit of the observed broadband spectrum of blazars using different emission models.

The attempt to perform a statistical fitting of blazar SED was first initiated by Mankuzhiyil et al. (2011) [19], where the authors fitted the multi-epoch, broadband SED of Mrk 421 using synchrotron and SSC processes. The fitting was performed using ψ^2 minimization technique incorporating Levenberg- Marquardt algorithm. In this work, we aim to fit the observed data with the agnpy models. For this, we use the modelling and fitting sub package provided within gammapy.

4 Modelling Mkn 421

4.1 Observations

Our case study deals with Markarian 421 (often referred as Mkn 421 of Mrk 421), one of the blazars closest to Earth, with a redshift of z=0.0308, that is around 120 Mpc. It was the first extragalactic object detected in the VHE range with Whipple [25] and also the first blazar detected in gamma-rays with the EGRET detector [17]. It is also the brightest blazar at X-ray energies, and hence is one of the most well studied objects at these energies [2], [5].

In April 2013, a huge increase of the flux of Mkn 421 was found in the X-rays by SWIFT and the gamma-ray VHE energy ranges by MAGIC. Although not the first time a flaring activity was detected, it was the first time that the flaring state could be tracked extensively at many different wavelengths with excellent sampling, thanks to the methods discussed in the section 3. This powerful AGN activity was observed for nine days by the MAGIC telescopes, the Fermi-LAT scanned the whole sky once every 3 hours, and there were many other dedicated X-Ray campaigns

as well. The VHE gamma-ray flux was two orders of magnitude greater that in the periods of low activity (quiescent state). The peak flux in the TeV range became 15 times higher than that of the Crab Nebula, i.e. about 30 times the typical flux of Mkn 421, and the optical continuum became bluer, which means that the non-thermal emission dominates even more on the host galaxy emission. The flare states consist of an extreme and wide variation during the active days as can be seen in figure 6. We can observe the strong positive correlation between VHE gamma-ray and X-ray peaks, and also small increases in fluxes in other energy ranges. This leads to the assumption that there are two types of components, as seen in [2]. The fast component, with variability periods of one hour as can be seen in [2], for which there is a high correlation between X-rays and VHE gamma-ray. This means that photons in these energy ranges are produced by the same electrons. On the other hand, the low components, with periods of several hours, have a lower degree of correlation, which may mean that the emission is produced by different elements (leptonic or hadronic), or by different populations. Our aim in this section is then to compare the flare and low activity states. In order to obtain the differences in the physical parameters of the AGN and thus try to understand the processes that may give rise to these sudden high-activity states.
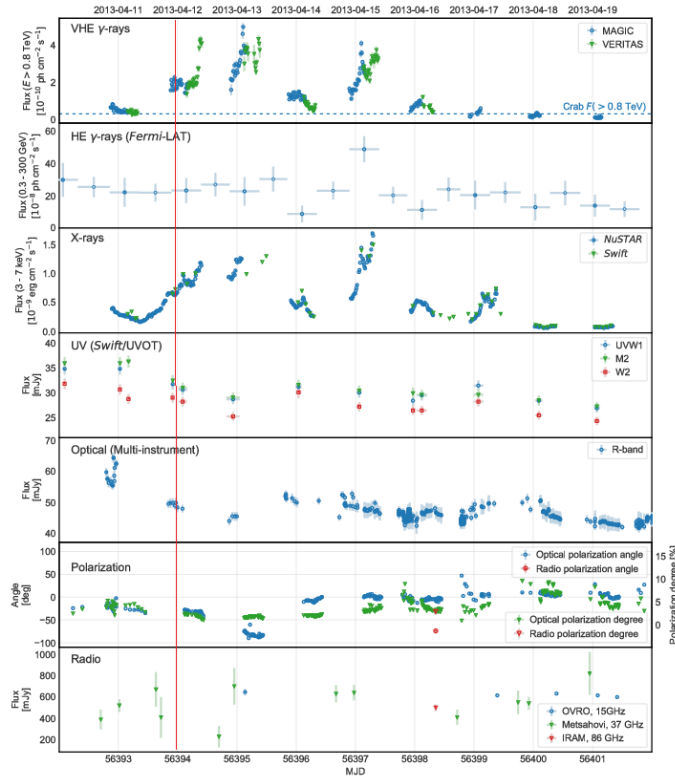

Figure 6: Multiwavelength light curve for Mrk 421 during the bright flaring activity in 2013 April taken from [2]. The red line corresponds to the day on which the data used in this work were obtained.

4.2 Modeling

4.2.1 Model description

To model our source Mkn 421 we will choose the leptonic model for modelling the data. This model consists of synchrotron emission to account for the hump which peaks between 10^{16} and 10^{17} Hz

(X-rays), and SSC emission for the second hump which peaks around 10^{25}, 10^{26} Hz (VHE gamma rays). The synchrotron and SSC SED is computed, following [8] and [10]. The region of emission will be the blob sketched in fig. 7a), and in our case we will not use any of the other emission regions as they are subdominant, e.g. bremsstrahlung radiation or black body radiation.

For the modelling, we firstly define the blob. It is a spherical plasmoid of radius R_b, streaming along the jet towards us with a bulk Lorentz factor Γ. Since it will have relativistic velocities, in order to correct the beaming effects, we will also define the relativistic Doppler factor δ_d which is given by:

$$\delta_d = \frac{1}{\Gamma(1 - \beta cos\theta)} \tag{14}$$

With β its speed in units of the speed of light, and θ the angle subtended by the speed and the line of sight. In the case of blazars, this angle is nearly zero so we can suppose $\delta_d \approx \Gamma = \sqrt{1/(1 - \beta^2)}$. We consider the electron distribution homogeneous and isotropic in the blob's rest frame. And we will take the Electron Energy Distribution (EED) as a broken power law (fig. 7b) with spectral indexes p1 and p2 that gives us the slope of each segment before and after the break given by the Lorentz factor γ_b, the lower and upper limits of the electrons energies are defined by the minimal and maximal Lorentz factors γ_{min} and γ_{max}. The normalisation factor of the EED is k_e. The differential equation which leads the evolution of the particle number density $N(\gamma, t)$ is:

$$\frac{\partial N}{\partial t} - \frac{\partial}{\partial \gamma}(P(\gamma) \cdot N) + \frac{N}{t_{esc}(\gamma)} = Q(\gamma)\Theta(\gamma - \gamma min)\Theta(\gamma_{max} - \gamma) \tag{15}$$

With $Q(\gamma)$ the power law distribution of electrons injected in the jet, and $P(\gamma)$ the radiative loss rate.

(a) AGN emission regions from [21]
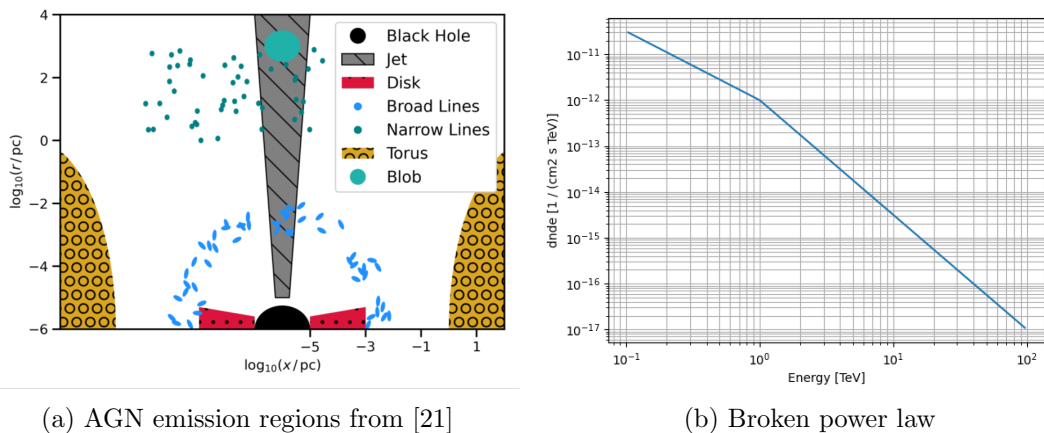
(b) Broken power law

Figure 7: In the left picture, the diagram of the AGN emission area and in the right picture, the EED with a broken power law

Finally we also have to account for the cosmological redshift (z) and the distance of the source (d_L). The blob is assumed to have a uniform magnetic field B, which is responsible for synchrotron and SSC radiation. This magnetic field will also establish whether we are in the equipartition condition. This condition implies that the magnetic energy density, which is responsible for enclosing the particles, is equal to the energy density of the particles which has a pressure function, expanding the particles, more about equipartition can be found in [28]. Using the energy density formulas, the equipartition condition results under the following equation:

$$P_{jet,e} = P_{jet,B} \rightarrow 2\pi R_b^2 \beta \Gamma^2 c m_e c^2 N_e = 2\pi R_b^2 \beta \Gamma^2 c \frac{B^2}{8\pi} \rightarrow m_e c^2 N_e = \frac{B^2}{8\pi} \tag{16}$$

Another parameter that we can calculate is the Larmor radius, which is the radius of the synchrotron motion of the electrons and can be easily obtained as [15]:

$$r_l = \frac{m_e \cdot v}{e \cdot B} \tag{17}$$

With v the speed of the electrons and e its charge.

4.2.2 Initial parameters

To start with we have to introduce some initial parameters that are close to the real ones to improve the fit convergence. For this we make use of observable variables such as the received frequency at which the SSC peak is obtained, the flux of incoming photons forming the SED of the source, or the timescale variability infered from the lightcurves. The first value that we can obtain is the spectral break γ_b, which is the cause of the SSC radiation peak, as seen in [2] it can be obtained as:

$$\gamma_b' = \frac{E_{SSC}}{\delta_d \cdot m_e c^2} \tag{18}$$

where E_{SSC} is the observed energy of the peak of the SSC, and m_e the electron mass. Knowing this value we can estimate (to within an order of magnitude) the minimum and maximum particle energies γ_{min} and γ_{max}, furthermore γ_{max} is chosen such that the highest energy synchrotron points do not have a cutoff. From opacity considerations, i.e. the VHE photons should not be self absorbed by the IR photons inside the emissionregion, we can also set a lower limit for the Lorentz bulk factor and thus for the Doppler factor. Relying on the large correlation of this flare state, we can assume that the IR-visible and VHE photons are produced in the same region, and as we can see in [2] this leads to a lower bound on the Doppler factor $\delta_d \leq 35$. Another parameter that we can estimate is the blob radius R_b' which can be constrained by the observational parameter t_{var}, which is the observed variability time scale. This can be interpreted as the time it takes for a perturbation to arrive from one end of the blob to the other. With t_{var} measured, the R_b' can be easily obtained as:

$$R_b' = c \cdot t_{var} \frac{\delta_d}{1+z} \tag{19}$$

For the spectral index as can be seen in [16], solving the equation 15 gives a broken power law solution with two spectral index p1 and p2 where $p1 = p$ and $p2 = p1 + 1$. So after the break the curve becomes steeper. With this EED we are setting a minimum and maximum energy for the electrons in the blob, taking into account that the more energy, the less electrons. The EED would be as:

$$dN_e' = d\gamma' \cdot V_b' \cdot k_e \left[\left(\frac{\gamma'}{\gamma_b'}\right)^{-p1} \cdot H(\gamma'; \gamma_{min}', \gamma_b') + \left(\frac{\gamma'}{\gamma_b'}\right)^{-p2} \cdot H(\gamma'; \gamma_b', \gamma_{max}') \right] \tag{20}$$

Where the primes denote the co-moving frame of the blob, V_b' is the volume of the blob, and H(x;a,b) is the Heaviside function which ensures null values outside our limits that go from γ_{min}' to γ_{max}'. For the last parameters, B and k_e we will use previous results as [2], [1].

The job of agnpy will therefore be to model the first hump of the SED with the synchrotron emission with the input data, and also to use the outgoing photons of this first emission as an incoming flux for modelling the second hump with the SSC radiation. Once established the initial parameters, we can plot them and see how far they are from the actual data, correcting them if necessary. Then we proceed to the fitting using gammapy, for that we will create a user defined model to interface agnpy with the gammapy fitting. We will start by loading the flux points, then setting as a theoretical model in gammapy the agnpy modelling of synchrotron and SSC, and introducing the initial parameters as discussed in section 4.2.2. Some of these parameters will be

introduced in logarithmic scale, in this way the fitting becomes easier for parameters that we expect to cover several orders of magnitude. Here we will be able to freeze and defreeze the variables as we wish. Parameters known accurately from other measurements, like redshift or distance, are kept frozen. Knowing how each variable affects the graph [6], this work of freezing variables will be easier. It is also possible to plot the covariance matrix which is investigated to check the correlations between the different parameters, and moreover to plot the fit statistic profiles for all fitted parameters and check if they are at a stable minimum (fig. 8 and fig. 9). The fitting consists of minimising the opposite of the likelihood function, i.e. trying to maximise the probability that the value of that parameter can generate the flux values obtained. As there may be more than one minimum for this function, it is important to set adequate initial values, to be close to the best minimum. Therefore, using these methods, we will try out various combinations and stick with the parameters that make the most physical sense and have the lowest total statistic error.

4.2.3   Quiescent state

The data used for the quiescent state are from [1], collected during Fermi's first 1.5 years of operation, from 2008 August 5 to 2010 March 12. We first started by obtaining a Doppler factor, we took the one obtained by Abdo et al. [1] while modelling the SED of Markarian 421 with a leptonic model in the quiescent state, which is 20. With this approximation we can already calculate the spectral break using equation 18, and with the peak of the SSC occuring at $E_{SSC,q} = h \cdot 6.07 \cdot 10^{25}$, with h the Planck constant:

$$\gamma'_{b,q} = \frac{E_{SSC,q}}{\delta_{d,q} \cdot m_e c^2} = 2.59 \cdot 10^4 \tag{21}$$

The time variability is of around 1 day, and the magnetic field obtained by Abdo et al. [1] is $B = 3.8 \cdot 10^{-2}G$. The spectral index would be of around $p1 = 2$ and $p2 = 3$. By introducing this initial parameters we firstly made an initial fitting with the parameter t_{var} frozen, obtaining a good approximation, and reasonable statistic profiles. With these first parameters we defreeze the t_{var} parameter obtaining a very precise fit even in the highest energies (10^{26} Hz and over), and very stable minimums in the statistic profiles. The final parameters are shown in table 1, and the modelling of the emission curve in figure 10. In fig. 8 we show the total statistics of the free parameters, which tells us if they are at a stable minimum and gives us an idea of their error.

Using eq. 16 we obtain the jet power of electrons and the magnetic field power:

$$P_{jet,e} = 1.69 \cdot 10^{44} erg/s \quad P_{jet,B} = 1.85 \cdot 10^{43} erg/s \tag{22}$$

And the Larmor radius, using eq. 17, will be:

$$r_l = 5.0 \cdot 10^5 cm \tag{23}$$

4.2.4   Flare state

The data used for the flare state comes from a private communication from MAGIC. It is an observation of 15min obtained on 12 April 2013, and the VHE data is already corrected for the EBL absorption. For this part we could start from the parameters obtained for the quiescent state, since we assume that the electrons come from the same region, the EED should not change much. We can think that the amount of electrons injected will be higher and that this is what causes the flare state, so we will have a higher k_e for this case. Again we can use equation 18 to obtain an approximation of the spectral break, for the flare state the peak of the SSC occurs at $E_{SSC,f} = h \cdot 7.97 \cdot 10^{25}$, and for a Doppler factor of 35:

$$\gamma'_{b,f} = \frac{E_{SSC,f}}{\delta_{d,f} \cdot m_e c^2} = 1.84 \cdot 10^4 \tag{24}$$
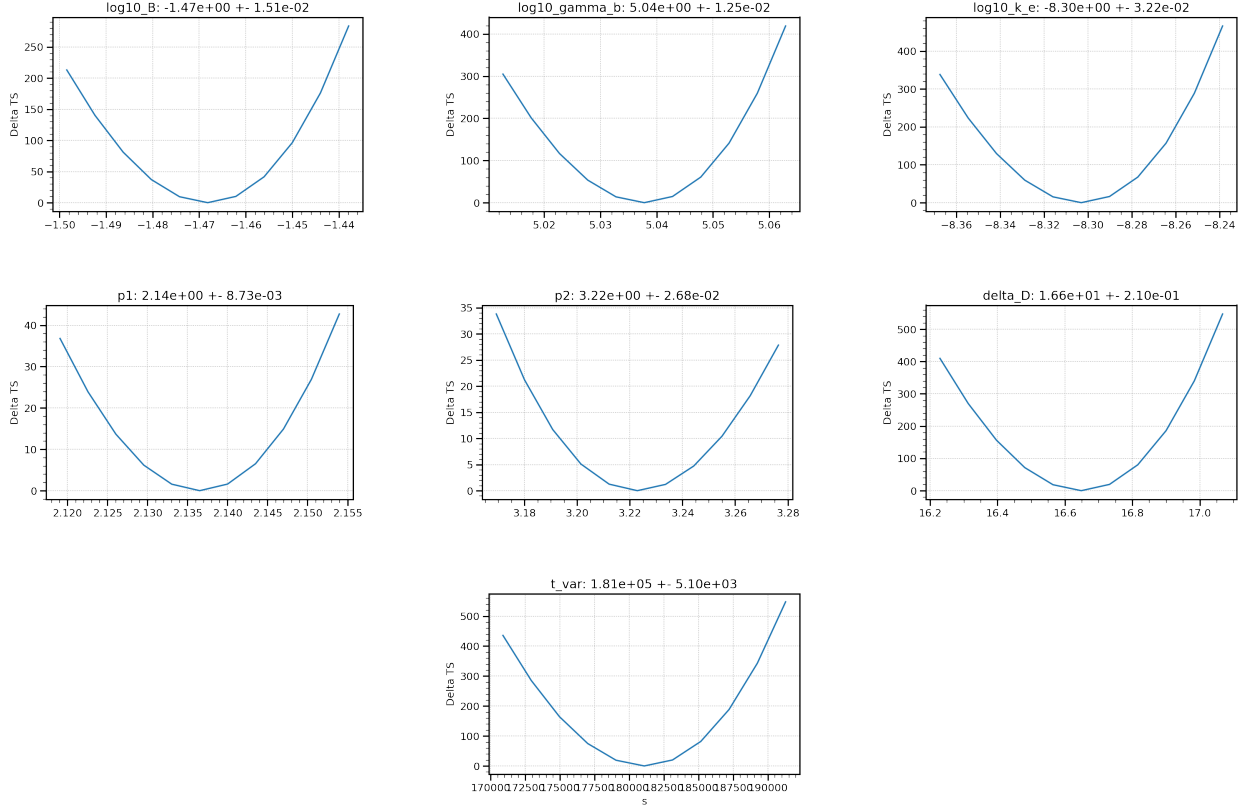
Figure 8: Plot statistics and the obtained error estimates of the parameters for the quiescent state

Also, remembering what we said in the previous section about the Doppler factor, we will initialise this parameter at $\delta_D = 35$. Due to this increase in the blob velocity and the data of its lightcurves [2] we infer a lower $t_{var} \approx 1$ hour, and a magnetic field of the same order as for the quiescent state. Introducing this initial parameters we obtain the fitted parameters in table 1, and its modelled curve in figure 10. In figure 9 we can see the total statistics of each parameter, in order to see their uncertainty and to verify that they are all in a stable minimum.

Using eq. 16 we obtain the jet power of electrons and the magnetic field power:

$$P_{jet,e} = 6.08 \cdot 10^{44} erg/s \quad P_{jet,B} = 7.54 \cdot 10^{42} erg/s \tag{25}$$

And the Larmor radius will be given by eq. 17 as:

$$r_l = 7.5 \cdot 10^5 cm \tag{26}$$

4.3 Discussion

Once the fitting of the data is done, we can remove the logarithmic scale to understand the parameters better, we can see them in the table (tab. 1). Looking at the final result of the fitting (fig. 10) we can see that the fit is quite close to the points in general for the chosen leptonic model (synchrotron ans SSC). This model provides a convenient way of understanding the different processes that take place to explain the emission of an AGN, and the scale and correlation of its parameters.

One of the few noticeable problems for both states that can be easily noticed in the residuals plot in fig. 11 and fig. 12, that above 10^{19} Hz (X-rays), the steep slope of the model at these
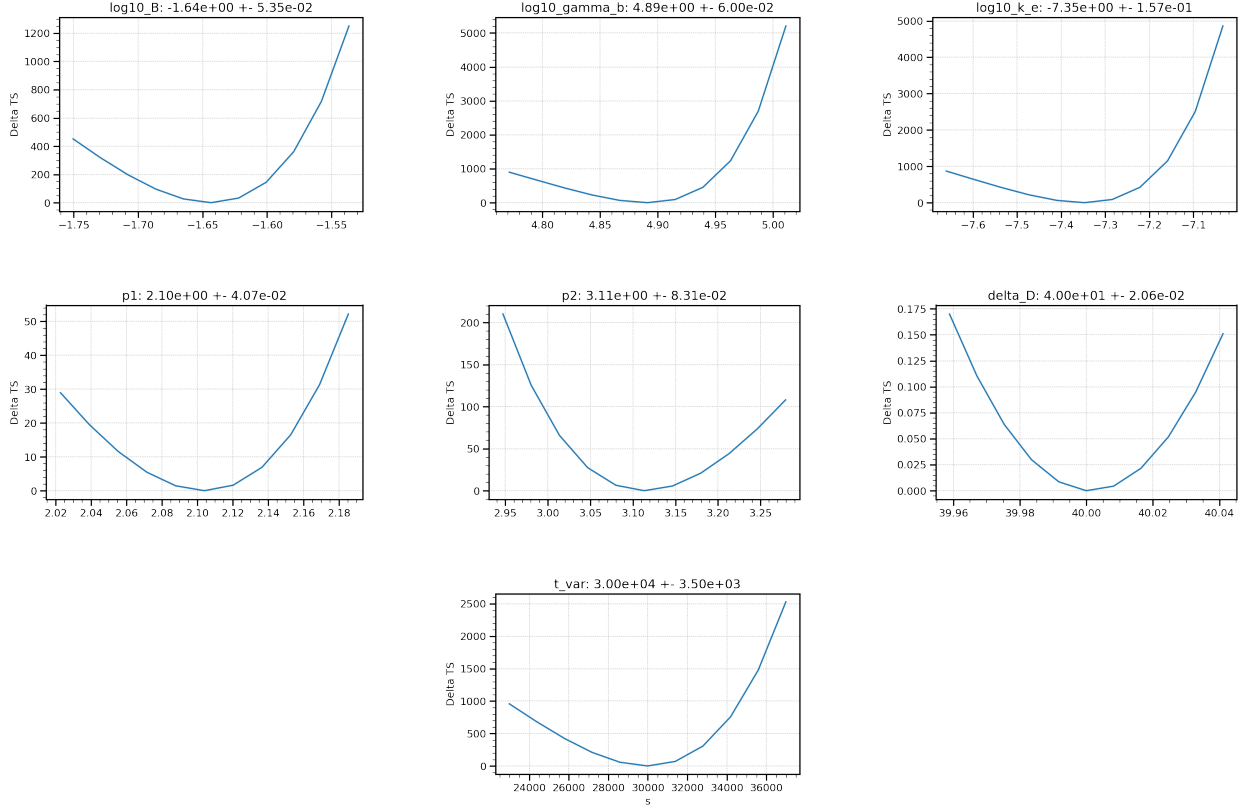
Figure 9: Plot statistics of the parameters for the flare state

frequencies makes that a minimum shift in the energies leads to a very large error. We can think that this mismatch is due to some other process that can take place at these frequencies such as external Compton. Another problem occurs above 10^{14} Hz for the quiescent state, where we see a point much higher than the rest. This deviation may be due to the light emitted by the galaxy in the visible. Since during the quiescent state the total flux is lower, photons that we cannot detect during the flare state show up in this lower luminosity state. We can also note that points below 10^9 Hz, i.e. radio emission, will not be adjusted. Because at these wavelengths the emission comes mainly from other components such as high star formation in the host galaxy [26].

As we can see in both the quiescent and flare state, the spectral indices satisfy $p2 = p1 + 1$. So the two states are in good agreement with the theoretical expectations of a particle number density with continous particle injection and cooling. Observing the obtained parameters we can conclude that the EED between the two states does not change excessively. The parameter p2 takes a lower value for the flare state, lower slope after the break, allowing a higher electron density with high energy. And γ_b is also lower in this high activity state producing the break in the EED earlier. But undoubtedly the EED parameter that changes the most between the two states is the normalisation of the electron spectrum. It is one order of magnitude higher for the flare state, this is consistent with expectations since we can assume that one of the main reasons for these increases in brightness is the higher mass accretion by the SMBH as discussed in sec. 2.1. Beyond the EED we have three other parameters that will vary significantly. To begin with, we observe the increase of the Doppler factor, and therefore of the velocity of the blob, which goes from $\Gamma = 16.6$ with a speed of $\beta_b = 0.9981$ in the quiescent state to $\Gamma = 40.0$ with a speed of $\beta_b = 0.9997$ for the flare state. This increase in the relativistic velocities illustrates the very high amount of energy that has
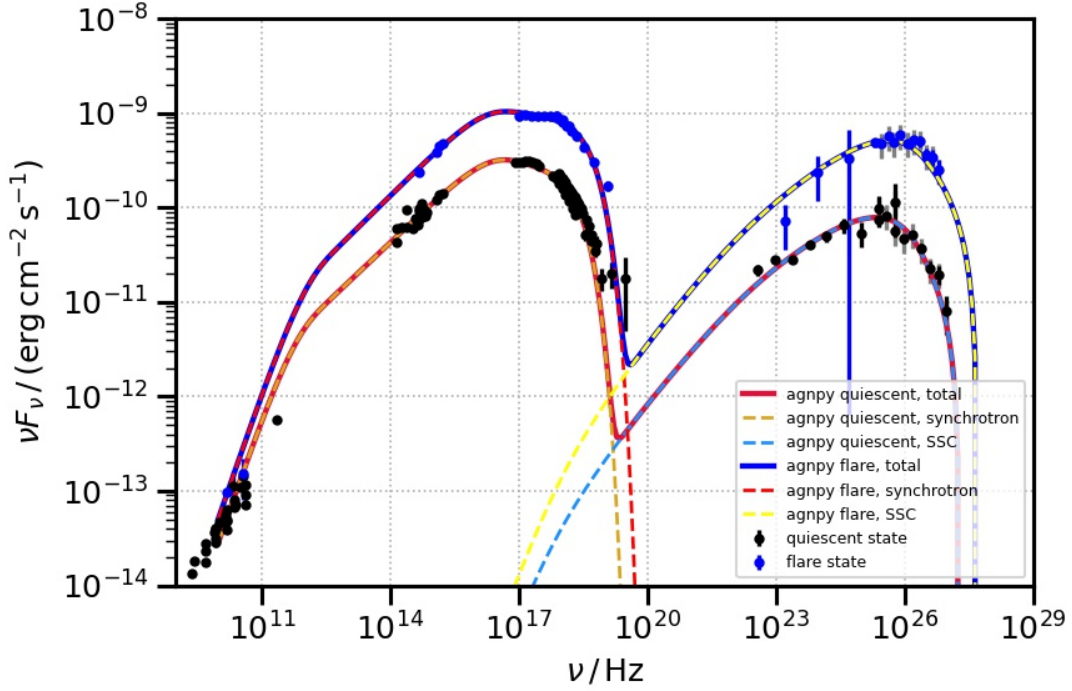
16

Figure 10: Fitting of the April 2013 flare state (upper curve) from [2] and the 2009 quiescent state (lower curve) from [1] with agnpy

the jet and therefore the SMBH during its flare states. In addition, the magnetic field decreases by 33%. Finally the t_{var} varies by an order of magnitude, in this case the timescale variability for the flare state will be of the order of 8 hours, and for the quiescent state of 2 days. These orders of magnitude are in good agreement with those inferred from the lightcurves, and those deduced in [2], and [1]. This reduction in variability times directly implies a reduction in the radius of the emission region, using the eq. 19, we can see that it would go from $8.74 \cdot 10^{16}$ cm for the quiescent state to $3.49 \cdot 10^{16}$ cm. This could be due to the fact that as the Doppler factor has increased and therefore the Lorentz factor Γ of the blob, the velocity of this spheroid increases and therefore its apparent size decreases.

	Quiescent	Flare			Quiescent	Flare
k_e (in cm^{-3})	$(5.0 \pm 0.3) \cdot 10^{-9}$	$(4.5 \pm 1.6) \cdot 10^{-8}$		z	$3.080 \cdot 10^{-2}$	$3.080 \cdot 10^{-2}$
p1	2.14 ± 0.01	2.10 ± 0.04		d_L (in cm)	$4.309 \cdot 10^{26}$	$4.309 \cdot 10^{26}$
p2	3.22 ± 0.03	3.11 ± 0.08		δ_D	16.6 ± 0.2	40.00 ± 0.02
γ_b	$(1.10 \pm 0.03) \cdot 10^5$	$(7.8 \pm 1.1) \cdot 10^4$		B (in G)	$(3.4 \pm 0.1) \cdot 10^{-2}$	$(2.3 \pm 0.3) \cdot 10^{-2}$
γ_{min}	$5.001 \cdot 10^2$	$5.200 \cdot 10^2$		t_{var} (in s)	$(1.81 \pm 0.05) \cdot 10^5$	$(3.00 \pm 0.45) \cdot 10^4$
γ_{max}	$1.000 \cdot 10^6$	$1.100 \cdot 10^6$				

Table 1: Parameters obtained for the quiescent state and for the flare state

Analysing the electron jet powers and magnetic field we can see that neither state is in equipartition. The quotient for the quiescent state differs from equipartition by one order of magnitude and for the flare by two. This may be a good argument to explain the short periods of variability of both states, as they are not emitting in a minimum energy state, as the equipartition one. When one of the two jet powers is higher, in both cases the electron jet power, the jet will tend to equipartition, thus giving up part of the particle energy in favour of the energy density of the
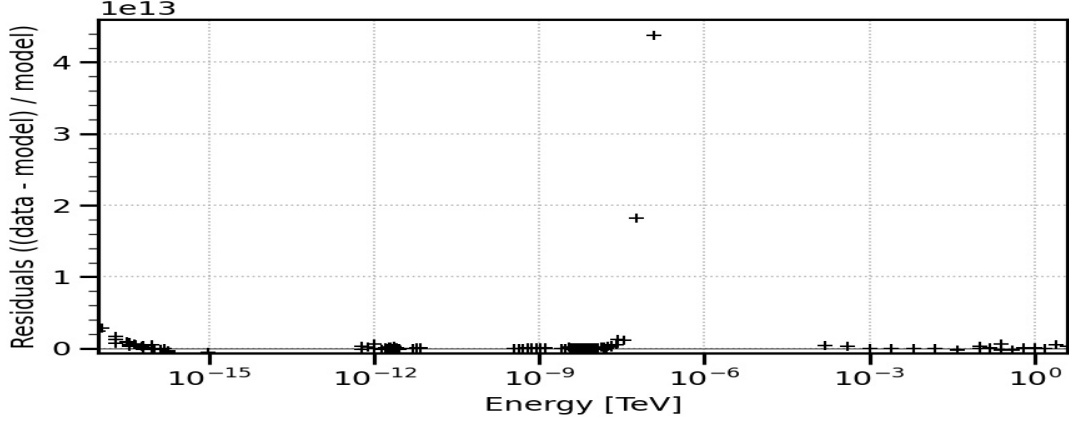
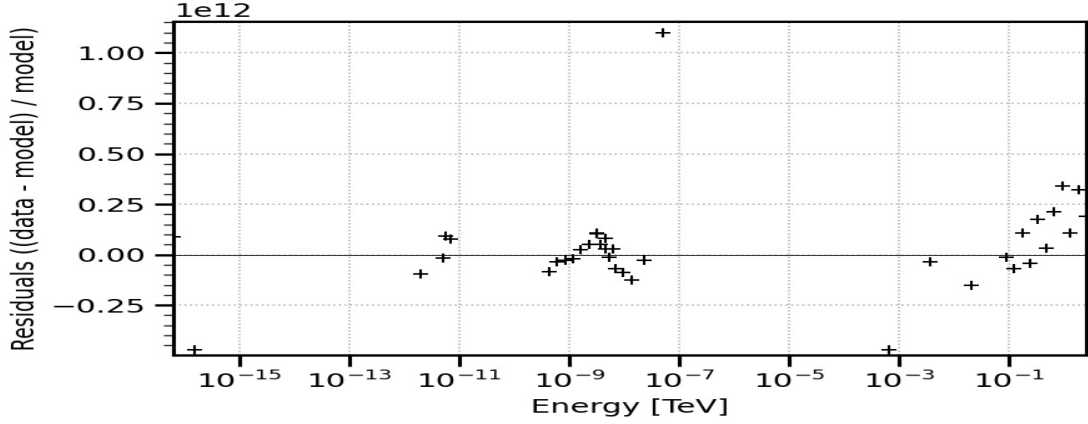Figure 11: Differential plot fit residuals in the quiescent state

Figure 12: Differential plot fit residuals in the flare state

magnetic field. The state that we modelled was not the highest flux state during this flare(as we can see in fig. 6) and it would be interesting to model the flare over different days and see how the physical parameters vary over the course of the flare. In the MAGIC paper [2], they deduced from the light curves that two distinct electron populations were needed to explain the flare state. These lightcurve measurements are practically instantaneous, i.e. over short periods of time, whereas our SED is averaged over several days, which means that two populations are no longer needed to model the emission, but only one. Similar conclusions were reached with respect to the number of emission zones in [29] and [13].

5   Conclusions

In this work we have analysed the broadband emission of the blazar Mkn421 at high energies for two states, the quiescent state and a flare state, using open source codes to model and fit the data. We have successfully used a leptonic model to explain the first peak in X-rays with synchrotron emission and the second peak in very high energy gamma rays with SSC.

The main difference between these two states is the flux received at these energies. The theory that best explains the emission of AGNs is by conversion of gravitational energy into radiative

18

energy. This is in agreement with the parameters obtained in this work, in which we find a higher number of electrons in the emitting blob for the flare state. Another of the most significant changes between the states is the increase of the Doppler factor of this emission region, which means that the jet not only accretes more mass but also ejects it at higher velocities. We have been able to explain the two processes by a single emission region for each case. We have also found that for the data obtained the blob is not in equipartition for either of the two states, the flare state being the one with a state furthest from equipartition.

Through this study I have learned the mechanism that governs the emission of AGNs, and the actual state of their interaction with the surrounding environment. It has been a very good approach to this beautiful branch of physics and to the study of mega structures in the universe.

name	value	unit	min	max	frozen	error
$log_{10}k_e$	-8.3025e+00		-2.000e+01	1.000e+01	False	3.219e-02
p1	2.1365e+00		-2.000e+00	5.000e+00	False	8.722e-03
p2	3.2227e+00		-2.000e+00	5.000e+00	False	2.677e-02
$log_{10}\gamma_b$	5.0377e+00		1.000e+00	6.000e+00	False	1.252e-02
$log_{10}\gamma_{min}$	2.6990e+00		0.000e+00	4.000e+00	True	0.000e+00
$log_{10}\gamma_{max}$	6.0000e+00		4.000e+00	8.000e+00	True	0.000e+00
z	3.0800e-02		1.000e-02	1.000e+00	True	0.000e+00
d_L	4.3094e+26	cm	1.000e+25	1.000e+33	True	0.000e+00
δ_D	1.6656e+01		0.000e+00	4.000e+01	False	2.097e-01
$log_{10}B$	-1.4684e+00		-4.000e+00	2.000e+00	False	1.513e-02
t_{var}	1.8091e+05	s	1.000e+01	3.142e+07	False	5.089e+03

Table 2: Parameters obtained by fitting the data of the quiescent state

name	value	unit	min	max	frozen	error
$log_{10}k_e$	-7.3468e+00		-2.000e+01	1.000e+01	False	1.568e-01
p1	2.1041e+00		-2.000e+00	5.000e+00	False	4.066e-02
p2	3.1134e+00		-2.000e+00	5.000e+00	False	8.308e-02
$log_{10}\gamma_b$	4.8912e+00		1.000e+00	6.000e+00	False	5.998e-02
$log_{10}\gamma_{min}$	2.7160e+00		0.000e+00	4.000e+00	True	0.000e+00
$log_{10}\gamma_{max}$	6.0414e+00		4.000e+00	8.000e+00	True	0.000e+00
z	3.0800e-02		1.000e-02	1.000e+00	True	0.000e+00
d_L	4.3094e+26	cm	1.000e+25	1.000e+33	True	0.000e+00
δ_D	4.0000e+01		0.000e+00	4.000e+01	False	2.056e-02
$log_{10}B$	-1.6434e+00		-4.000e+00	2.000e+00	False	5.351e-02
t_{var}	2.9987e+04	s	1.000e+01	3.142e+07	False	3.499e+03

Table 3: Parameters obtained by fitting the data of the flare state

	Quiescent	Flare
k_e (in cm^{-3})	$(5.0 \pm 0.3) \cdot 10^{-9}$	$(4.5 \pm 1.6) \cdot 10^{-8}$
p1	2.14 ± 0.01	2.10 ± 0.04
p2	3.22 ± 0.03	3.11 ± 0.08
γ_b	$(1.10 \pm 0.03) \cdot 10^5$	$(7.8 \pm 1.1) \cdot 10^4$
γ_{min}	$5.001 \cdot 10^2$	$5.200 \cdot 10^2$
γ_{max}	$1.000 \cdot 10^6$	$1.100 \cdot 10^6$
z	$3.080 \cdot 10^{-2}$	$3.080 \cdot 10^{-2}$
d_L (in cm)	$4.309 \cdot 10^{26}$	$4.309 \cdot 10^{26}$
δ_D	16.6 ± 0.2	40.00 ± 0.02
B (in G)	$(3.4 \pm 0.1) \cdot 10^{-2}$	$(2.3 \pm 0.3) \cdot 10^{-2}$
t_{var} (in s)	$(1.81 \pm 0.05) \cdot 10^5$	$(3.00 \pm 0.45) \cdot 10^4$

6   Bibliography

References

[1]   A. A. Abdo et al. "FERMI LARGE AREA TELESCOPE OBSERVATIONS OF MARKAR-IAN 421: THE MISSING PIECE OF ITS SPECTRAL ENERGY DISTRIBUTION". In: *The Astrophysical Journal* 736.2 (July 2011), p. 131. DOI: 10.1088/0004-637x/736/2/131. URL: https://doi.org/10.1088%2F0004-637x%2F736%2F2%2F131.

[2]   V. A. Acciari et al. "Unraveling the Complex Behavior of Mrk 421 with Simultaneous X-Ray and VHE Observations during an Extreme Flaring Activity in 2013 April". In: 248.2, 29 (June 2020), p. 29. DOI: 10.3847/1538-4365/ab89b5. arXiv: 2001.08678 [astro-ph.HE].

[3]   *Agnpy docs*. URL: https://agnpy.readthedocs.io/en/latest/#.

[4]   Robert Antonucci. "The Glowing Dusty Heart of a hidden quasar". In: *Nature News* (Feb. 2022). URL: https://www.nature.com/articles/d41586-022-00380-4.

[5]   Pedro Antoranz Canales et al. "Observations of Markarian 421 with the MAGIC telescope". In: *Astrophysical journal* 663.1 (Par (July 2007), pp. 125–138. ISSN: 0004-637X. DOI: 10.1086/518221. URL: http://dx.doi.org/10.1086/518221.

[6]   Steven D. Bloom and Alan P. Marscher. "An Analysis of the Synchrotron Self-Compton Model for the Multi–Wave Band Spectra of Blazars". In: 461 (Apr. 1996), p. 657. DOI: 10.1086/177092.

[7]   Christoph Deil et al. *Gammapy - A prototype for the CTA science tools*. 2017. DOI: 10.48550/ARXIV.1709.01751. URL: https://arxiv.org/abs/1709.01751.

[8]   Charles D. Dermer and Govind Menon. *High Energy Radiation from Black Holes: Gamma Rays, Cosmic Rays, and Neutrinos*. 2009.

[9]   Primack J.R. Domínguez A. and Bell T.E. "All the light there ever was". In: (June 2015).

[10]   Justin D. Finke, Charles D. Dermer, and Markus Böttcher. "Synchrotron Self-Compton Analysis of TeV X-Ray-Selected BL Lacertae Objects". In: 686.1 (Oct. 2008), pp. 181–194. DOI: 10.1086/590900. arXiv: 0802.1529 [astro-ph].

[11]   *Gamma-Ray Group*. URL: https://www.ifae.es/groups/gammaray/.

[12]   *Gammapy*. URL: https://gammapy.org/.

[13] Pranjupriya Goswami et al. "Unfolding the X-ray spectral curvature of Mkn 421 for further clues". In: *Monthly Notices of the Royal Astronomical Society* 499.2 (Oct. 2020), pp. 2094–2103. DOI: 10.1093/mnras/staa3022. URL: https://doi.org/10.1093%2Fmnras%2Fstaa3022.

[14] *H.E.S.S.* URL: https://www.mpi-hd.mpg.de/hfm/HESS/.

[15] John David Jackson. *Classical Electrodynamics, 3rd Edition*. 1998.

[16] N. S. Kardashev. "Nonstationarity of Spectra of Young Sources of Nonthermal Radio Emission". In: 6 (Dec. 1962), p. 317.

[17] Y. C. Lin et al. "Detection of High-Energy Gamma-Ray Emission from the BL Lacertae Object Markarian 421 by the EGRET Telescope on the Compton Observatory". In: 401 (Dec. 1992), p. L61. DOI: 10.1086/186671.

[18] Alicia López-Oramas. "Multi-year Campaign of the Gamma-Ray Binary LS I +61∘ 303 and Search for VHE Emission from Gamma-Ray Binary Candidates with the MAGIC Telescopes". In: (Apr. 2015). DOI: 10.13140/RG.2.1.4140.4969.

[19] Nijil Mankuzhiyil et al. *Environment and properties of emitting electrons in blazar jets: Mrk 421 as a laboratory*. 2011. DOI: 10.48550/ARXIV.1111.0265. URL: https://arxiv.org/abs/1111.0265.

[20] *Markarian 421*. URL: http://tevcat.uchicago.edu/?mode=1&showsrc=75.

[21] C. Nigro et al. "agnpy: An open-source python package modelling the radiative processes of jetted active galactic nuclei". In: *Astronomy &amp Astrophysics* 660 (Apr. 2022), A18. DOI: 10.1051/0004-6361/202142000. URL: https://doi.org/10.1051%2F0004-6361%2F202142000.

[22] *NuSTAR*. URL: https://www.nustar.caltech.edu/page/about.

[23] Vaidehi S. Paliya, S. Sahayanathan, and C. S. Stalin. "MULTI-WAVELENGTH OBSERVATIONS OF 3C 279 DURING THE EXTREMELY BRIGHT GAMMA-RAY FLARE IN 2014 MARCH–APRIL". In: *The Astrophysical Journal* 803.1 (Apr. 2015), p. 15. DOI: 10.1088/0004-637x/803/1/15. URL: https://doi.org/10.1088%2F0004-637x%2F803%2F1%2F15.

[24] Bradley M. Peterson. *An Introduction to Active Galactic Nuclei*. 1997.

[25] M. Punch et al. "Detection of TEV photons from the active Galaxy Markarian 421". In: *Nature News* (1992). URL: https://www.nature.com/articles/358477a0#citeas.

[26] Radcliffe, J. F. et al. "The radio emission from active galactic nuclei". In: *A&A* 649 (2021), p. L9. DOI: 10.1051/0004-6361/202140791. URL: https://doi.org/10.1051/0004-6361/202140791.

[27] George B. Rybicki and Alan P. Lightman. *Radiative Processes in Astrophysics*. 1986.

[28] B. Sunder Sahayanathan. *Broadband spectral modelling of bent jets of Active Galactic Nuclei*. 2011. DOI: 10.48550/ARXIV.1109.0618. URL: https://arxiv.org/abs/1109.0618.

[29] A. Sinha et al. "Long-term study of Mkn 421 with the HAGAR Array of Telescopes". In: *Astronomy &amp Astrophysics* 591 (June 2016), A83. DOI: 10.1051/0004-6361/201628152. URL: https://doi.org/10.1051%2F0004-6361%2F201628152.

[30] *The Fermi gamma-ray space telescope*. URL: https://fermi.gsfc.nasa.gov/.

[31] *The MAGIC telescopes*. URL: https://www.iac.es/es/observatorios-de-canarias/telescopios-y-experimentos/magic-telescopes.

[32] *The Neil Gehrels SWIFT observatory*. URL: https://swift.gsfc.nasa.gov/.

[33]   *VERITAS*. URL: https://veritas.sao.arizona.edu/.